ASME Journal of Dynamic Systems, Measurement, and Control
Online journal at:
https://asmedigitalcollection.asme.org/dynamicsystems

Convex Optimization Based Design of Finite Impulse Response Filters for Reference Shaping

Adrian Stein
Department of Mechanical and Aerospace Engineering,
University at Buffalo (SUNY),
Buffalo, NY 14260-4400
e-mail: astein3@buffalo.edu

Tarunraj Singh[1]
Professor
Department of Mechanical and Aerospace Engineering,
University at Buffalo (SUNY),
Buffalo, NY 14260-4400
e-mail: tsingh@buffalo.edu

This paper explores design of finite impulse response (FIR) filters for controlling underdamped systems while dealing with uncertainties in model parameters. By setting magnitude constraints in the frequency domain within a convex programing framework, it ensures that dominant resonant modes are attenuated at the end of the maneuver, high-frequency unmodeled modes are not excited, and there is no inordinate accentuation of frequencies in the passband of the filter. A mobile platform with an attached flexible beam serves as a testbed to validate the designs for rest to rest maneuvers, demonstrating how different cost functions of error between the desired and optimized magnitude response affect the filter performance. The study also examines robustness in the notch area by shifting the natural frequencies of the system by shifting a tip mass at the free end of the beam. The total energy at the final maneuver time of the first three system modes is calculated as a vibration suppression metric and is used to compare established input shapers with the proposed finite impulse response filters. [DOI: 10.1115/1.4065702]

Keywords: FIR filter, convex optimization, gantry crane, Euler–Bernoulli beam

1 Introduction

Feed-forward control is a well-established technique for vibration suppression in wafer scanners [1–3], cranes [4], assembly robots in the automotive industry [5], flexible manipulators [6], and in hard drives [7]. One method to design control constrained time-optimal [8] or fuel-optimal [7] profiles is to pose them as the design of time-delay filters (TDF) which can be designed for a single mode or multiple modes [9]. The TDFs break a step input into a sequence of delayed steps with the aim of eliminating residual vibrations and can be used to design reference shapers for stable underdamped linear systems in the continuous time domain [10] or in discrete-time [11]. These input-shaper designs are posed in the continuous time, while finite impulse response (FIR) filters are a prime example for a feed-forward controller design in discrete time. The main subgroups of FIR filters are linear and nonlinear phase filter, while the Parks–McClellan algorithm which was presented in Ref. [12] is one of the most famous algorithms to achieve linear phase characteristics [13]. Linear phase can be realized by enforcing symmetry or antisymmetry about the midpoint of the filter coefficients. Furthermore, complex filter coefficients can be used to design FIR filter as in Ref. [14]. In recent years, many contributions have shown that FIR filters can be designed by solving a convex optimization problem, while characteristics like linear phase behavior can still be guaranteed [15,16]. The main feature of a convex problems is that the solution of the optimization problem guarantees the cost to be the global minimum [17] and additional constraints like a DC-gain of unity or upper and lower limits on the variables can easily be enforced [13]. An implementation of embedded real-time FIR filter for vibration control can be found in Ref. [6].

The Chebyshev design is a minimax technique and is a widely used approach to design FIR filters, where the difference between the desired and the realizable values, so-called error, is solved as a L_∞ norm problem [18]. Preuss [19] states that there are different approaches to optimize for the error, for instance, as an elliptical cost function, which permits imposing greater weight on the phase or the magnitude constraint which was used by Lai et al. [20]. Aggarwal et al. [18] use the L_1 norm of the error as the cost, which lead to a diamond-shaped cost function contour. Qin [21] uses different polygons as a cost function. Davidson [13] exploits the magnitude responses where lower and upper constraint are enforced as spectral masks.

This work focuses on vibration suppression of multimode systems where only the magnitude constraints of the filter are considered, resulting in nonlinear phase filters. The FIR filter coefficients are assumed to be real. Since the target applications are underdamped systems, one metric to evaluate how well a filter is performing with regards to attenuating vibrations, is the terminal time residual energy. For applications where the focus lies on the attenuation of single dominant modes, like in gantry crane systems, a simple TDF for single mode cancelation can be used. However, these filters might excite higher modes because of the abrupt changes in the control profiles over time. To account for higher modes, for which the natural frequencies might be unmodeled, low-pass FIR filters with a notch can replace the TDFs. Solely focusing the optimization of the FIR filter on the residual energy would only target specific natural

[1]Corresponding author.

Contributed by the Dynamic Systems Division of ASME for publication in the Journal of Dynamic Systems, Measurement, and Control. Manuscript received April 28, 2023; final manuscript received May 21, 2024; published online June 20, 2024. Assoc. Editor: Weidong Zhu.

frequencies, whereas our approach aims to attenuate unmodeled higher modes as well. The notch is placed around the known dominant natural frequency and the higher modes are placed in the stopband. Different notch low-pass FIR filters are designed where the cost function contour could be a rectangle, diamond, circle, square or an ellipse, which are shapes to ensure convexity of the optimization problem. Different scenarios to account for variations in the number of filter elements, transition widths or weights are presented. Additionally robustness is studied in the notch area, and validated with experiments. This paper considers a tabletop gantry crane driven by stepper motors which permits commanding the position of the trolley. An attached flexible beam with a tip mass will include multiple underdamped modes in the tip displacement dynamics, making it an ideal testbed to validate the proposed algorithms. The tip mass is realized by a pair of attached magnets which could be slid along the beam to manifest model uncertainties.

The paper starts in Sec. 2 with the formulation of a convex optimization problem to determine the FIR filter. This is followed by a detailed development in Sec. 3 of the model of an Euler–Bernoulli beam with a tip mass and the experimental setup which uses strain gauges to evaluate the performance of the feed-forward controllers. Section 4 presents simulation and experimental results dealing with multiple implementations of the controllers. Section 5 concludes the paper.

2 Finite Impulse Response Design

An FIR filter can be represented in discrete time as $H(z) = \sum_{n=0}^{N-1} h[n]z^{-n}$, where the number of filter elements are N, h is the filter coefficients, and z is a complex number. Using $z = e^{j\omega_l T_s}$, we can state

$$H(e^{j\omega_l T_s}) = \sum_{n=0}^{N-1} h[n]e^{-jn\omega_l T_s} \tag{1}$$

$$= \sum_{n=0}^{N-1} h[n](\cos(n\omega_l T_s) - j\sin(n\omega_l T_s)) \tag{2}$$

where $l \in [0, L]$, L is the number of sampled frequencies ($L = 15N$), and $\omega_l \in [0, \pi]$ is the frequency. The sampling time T_s determines which frequencies can be captured in the FIR design. For smaller sampling intervals T_s, the FIR filter can actively be optimized for higher frequencies. If the number of filter elements is left constant but T_s decreases, the largest reachable frequency in the spectrum becomes greater, resulting in an increasing distance between each sample and therefore in a generally poorer curve fit in between frequency samples. The Chebyshev approach, which is a minimax design is often used to pose the design of the FIR filter in a convex programing framework, and can be written as

$$\min_{h[n]} \max_{\omega_l} |H(\omega_l) - H_d(\omega_l)|, \; l \in [0, L] \tag{3}$$

where $H(\omega)$ and $H_d(\omega)$ are the actual and desired transfer functions, respectively. Since the Chebyshev approximation considers the L_∞-norm, we introduce a different weighted error function to account for various norms

$$\underset{h[n]}{\text{minimize}} : \quad \delta \tag{4}$$

$$\text{subject to} : \quad ||W(\omega_l)(\Gamma(\omega_l)h - b_i(\omega_l))||_p \leq \delta \tag{5}$$

$$\text{where} : \quad \Gamma(\omega_l) = \begin{bmatrix} 1 & \cos(\omega_l) & \cdots & \cos((N-1)l) \\ 0 & \sin(\omega_l) & \cdots & \sin((N-1)l) \end{bmatrix} \tag{6}$$

$$b_i(\omega_l) = \begin{bmatrix} \text{Re}(H_d(\omega_l)) \\ \text{Im}(H_d(\omega_l)) \end{bmatrix} \tag{7}$$

$$h = \begin{bmatrix} h_0 & h_1 & \cdots & h_{n-1} \end{bmatrix}^{\text{T}} \tag{8}$$

where $W(\omega_l)$ is a non-negative weighting function, p defines the norm, and δ is the maximum error between the desired and optimized magnitude response $M(\omega) = ||\Gamma(\omega)h||$. Figure 1 illustrates the different cost functions as L_1, L_2, and L_∞ in complex plane which constrains the location of the complex vector. L_1, L_2 or L_∞ norm is used in the passband and the L_2 norm in the stopband. Another cost function is a rotated ellipse and can be seen in the following equation:

$$W(\omega_l)\left(\frac{\left(\text{Re}(\Gamma(\omega_l)h - H_d(\omega_l))\cos\left(\phi + \frac{\pi}{2}\right) + \text{Im}(\Gamma(\omega_l)h - H_d(\omega_l))\sin\left(\phi + \frac{\pi}{2}\right)\right)^2}{a_e^2} \ldots \right.$$
$$\left. \ldots + \frac{\left(\text{Re}(\Gamma(\omega_l)h - H_d(\omega_l))\sin\left(\phi + \frac{\pi}{2}\right) - \text{Im}(\Gamma(\omega_l)h - H_d(\omega_l))\cos\left(\phi + \frac{\pi}{2}\right)\right)^2}{b_e^2}\right) \leq \delta \tag{9}$$

where a_e and b_e represent the major and minor axis of the ellipse, respectively. The convexity of the cost function is preserved and the angle ϕ can simply be determined from the frequency of the desired transfer function via

$$\phi = \arctan\left(\frac{\text{Im}(H_d(\omega_l))}{\text{Re}(H_d(\omega_l))}\right) \tag{10}$$

It should be noted that the ratio between the major and minor axis needs to be prescribed before the optimization process starts. Similar to the elliptic cost function, a rectangular cost function can be introduced, where the cost function is

$$W(\omega_l)R\left(\begin{bmatrix} \text{Re}(\Gamma(\omega_l)h) \\ \text{Im}(\Gamma(\omega_l)h) \end{bmatrix} - \begin{bmatrix} \text{Re}(H_d(\omega_l)) \\ \text{Im}(H_d(\omega_l)) \end{bmatrix}\right) \leq \begin{bmatrix} a_r \\ b_r \end{bmatrix}\delta \tag{11}$$

$$W(\omega_l)R\left(\begin{bmatrix} \text{Re}(H_d(\omega_l)) \\ \text{Im}(H_d(\omega_l)) \end{bmatrix} - \begin{bmatrix} \text{Re}(\Gamma(\omega_l)h) \\ \text{Im}(\Gamma(\omega_l)h) \end{bmatrix}\right) \leq \begin{bmatrix} a_r \\ b_r \end{bmatrix}\delta \tag{12}$$

$$R = \begin{bmatrix} \cos\left(-\phi + \frac{\pi}{2}\right) & -\sin\left(-\phi + \frac{\pi}{2}\right) \\ \sin\left(-\phi + \frac{\pi}{2}\right) & \cos\left(-\phi + \frac{\pi}{2}\right) \end{bmatrix} \tag{13}$$

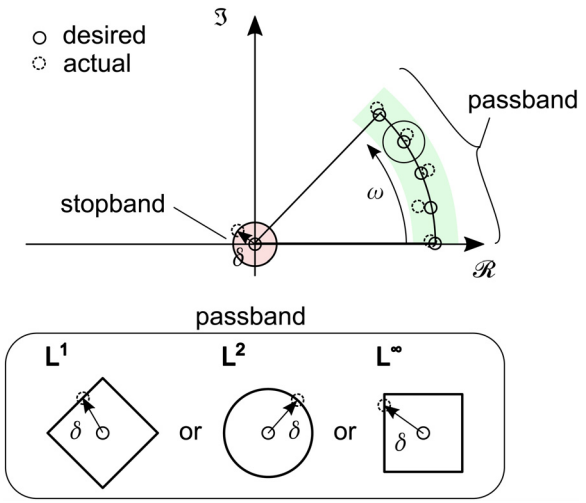

Fig. 1 Convex optimization of a finite impulse filter when looking at it in the complex plane

The angle ϕ is calculated as in the elliptic cost function with Eq. (10) and R is the rotation matrix. a_r is the width and b_r is the height of the rectangle as can be seen in Fig. 2. For the results presented in this paper, we assume $a_e = a_r = 2$ and $b_e = b_r = 1$. The velocity of the trolley of the gantry crane used to validate the designs is constrained to a maximum velocity $v_{\max}$. Therefore, the optimizer needs to ensure that the FIR filter never exceeds $v_{\max}$ at any time instant. Additionally, all FIR coefficients are required to sum up to 1, to force the DC-gain of the system to be unity. These constraints result in

$$-\mathbf{1}_{N\times 1} \leq \underbrace{\begin{bmatrix} 1 & 0 & \cdots & 0 \\ 1 & 1 & \ddots & \vdots \\ \vdots & & \ddots & 0 \\ 1 & 1 & \cdots & 1 \end{bmatrix}}_{N\times N} h \leq \mathbf{1}_{N\times 1}; \quad \sum_{i=0}^{N-1} h_i = 1 \tag{14}$$

2.1 Finite Impulse Response With a Notch Filter. To cancel the dominant mode for a point-to-point maneuver, a notch is added to the low-pass FIR filter. It is well known that the notch cannot be infinitesimally narrow, because this would lead to ripples around its corners (Gibbs phenomenon). Similar to the transition from the passband to the stopband tr, another transition band from the passband to the notch tr_{notch} is introduced. Figure 3 illustrates the ideal FIR filter with a notch, which targets the underdamped modes within the passband. The highlighted green, blue, and red area represent the 1. pass and 2. pass and stopband, respectively. The unmodeled dynamics are presumed to lie in the stopband to prevent exciting them. It should be noted that one can include multiple notches in the passband to target well modeled low frequency modes. A notch constraint can be added to the FIR design as

$$||\Gamma(\omega_{\text{notch}})h||_2 \leq 1e^{-5} \tag{15}$$

where ω_{notch} is the target frequency to place a notch. Each mode is modeled as a resonance of a second-order system and therefore the notch is placed at $\omega_{\text{notch}} = \omega_{n,1}\sqrt{1-2\zeta_1^2}$, where the natural frequency $\omega_{n,1}$ and the damping ratio ζ_1 need to be specified. Note that $1e^{-5}$ is considered as a reasonable attenuation in the magnitude response of a filter.

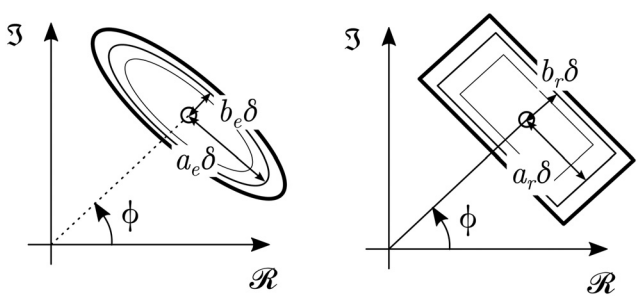

Fig. 2 Rectangular and elliptical cost function in the complex plane for FIR coefficients

2.2 Quality of a Notch. A metric to quantify the quality of a notch is proposed which entails calculating the area under the magnitude response over a specified range of frequencies. Figure 4 shows that the integration bound is twice tr_{notch}, where the black-dotted and solid line represent the desired and optimized notch realization, respectively. The calculation of the area under the magnitude response Q and normalized area Q_n can be written as

$$Q = \int_{\omega_{\text{notch}}-\text{tr}_{\text{notch}}}^{\omega_{\text{notch}}+\text{tr}_{\text{notch}}} |\sum_{n=0}^{N} h[n](\cos(n\omega T_s)\ldots \\ \ldots - j\sin(n\omega T_s))|d\omega \tag{16}$$

$$Q_n = \frac{Q}{2\text{tr}_{\text{notch}}} \tag{17}$$

The trapezoidal numerical integration rule is used to calculate Eq. (16). Q_n allows to fairly characterize robustness in terms of the quality of the notch. A smaller Q_n indicates a better quality of the notch.

3 Experimental Setup and Euler–Bernoulli Beam Theory

The experiments were conducted on a $8' \times 4' \times 3'$ gantry crane system where the trolley is attached to a stepper motor via a timing belt, which can be seen in Fig. 5. The strain gauges are placed near the clamped end of the beam where four of them are connected in a Wheatstone bridge circuit. The motion of the trolley is constrained by the maximum number of steps per time instant (velocity constraint). With the driver set to 400 steps per revolution, the trolley displaces by 40 mm per motor revolution. For this setup, it is found that the maximum velocity of the trolley is $v_{\max} = 240$ mm/s.

3.1 Euler–Bernoulli Beam. Figure 6 illustrates the Euler–Bernoulli beam model where one end is clamped to the trolley and the other end is free with a tip mass. The tip mass, realized

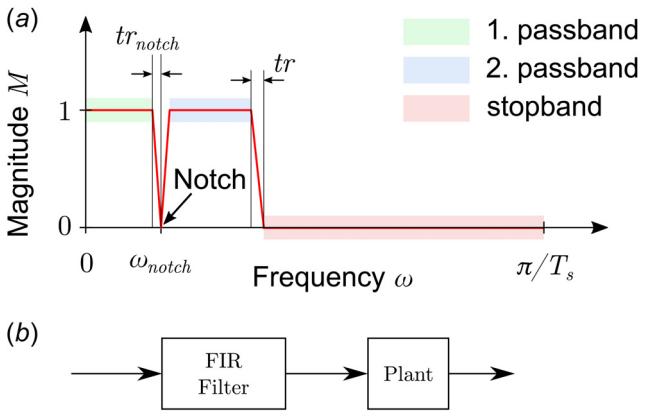

Fig. 3 (*a*) Desired magnitude of low-pass FIR filter with a notch and (*b*) block diagram of an FIR filter and a plant

by a pair of magnets, can be displaced in a vertical direction to emulate uncertainty. This feature will be used in Sec. 4.3 for robustness studies of the FIR notch filter. The Euler–Bernoulli beam is modeled with the partial differential equation

$$YI\frac{\partial^4 w(x,t)}{\partial x^4} + \rho A\frac{\partial^2 w(x,t)}{\partial t^2} = 0 \tag{18}$$

where $w(x, t)$ represents the deflection of the beam and Y, I, ρ, and A represent the Young's modulus, area moment of inertia, density, and cross section area of the beam ($A = qk$), respectively. For a clamped-free beam, the following boundary conditions apply [22]:

$$w(0,t) = 0 \tag{19}$$

$$\left.\frac{\partial w(x,t)}{\partial x}\right|_{x=0} = 0 \tag{20}$$

$$\begin{aligned} &YI\left.\frac{\partial^2 w(x,t)}{\partial x^2}\right|_{x=L} + \left(I_t + m_t\frac{L_t^2}{4}\right)\ldots \\ &\ldots\frac{\partial^2}{\partial t^2}\left(\left.\frac{\partial w(x,t)}{\partial x}\right)\right|_{x=L} + m_t\frac{L_t}{2}\left.\frac{\partial^2 w(x,t)}{\partial t^2}\right|_{x=L} = 0 \end{aligned} \tag{21}$$

$$\begin{aligned} &YI\frac{\partial}{\partial x}\left(\left.\frac{\partial^2 w(x,t)}{\partial x^2}\right)\right|_{x=L} - m_t\left.\frac{\partial^2 w(x,t)}{\partial t^2}\right|_{x=L}\ldots \\ &\ldots - m_t\frac{L_t}{2}\frac{\partial^2}{\partial t^2}\left(\left.\frac{\partial w(x,t)}{\partial x}\right)\right|_{x=L} = 0 \end{aligned} \tag{22}$$

The subscript "t" is used for parameters associated with the tip mass. The moments of inertia can be calculated as follows $I = \left(kq^3/12\right)$ and $I_t = (m_t/12)\left(L_t^2 + (2q_t + q)^2\right)$. Note that the tip with the magnets is not modeled as a point mass and has a moment of inertia I_t, corresponding to the mass moment of inertia of two magnets and the enclosed beam. Separation of variables permits writing the deflection of the beam $w(x, t)$ with its closed form representation of the mode shapes [23] as

$$w(x,t) = \sum_{i=1}^{\infty}\Phi_i(x)T_i(t) \tag{23}$$

$$\begin{aligned} \Phi_i(x) = K_{1,i}\cosh\left(\frac{\lambda_i x}{L}\right) + K_{2,i}\cos\left(\frac{\lambda_i x}{L}\right)\ldots \\ \ldots + K_{3,i}\sinh\left(\frac{\lambda_i x}{L}\right) + K_{4,i}\sin\left(\frac{\lambda_i x}{L}\right) \end{aligned} \tag{24}$$

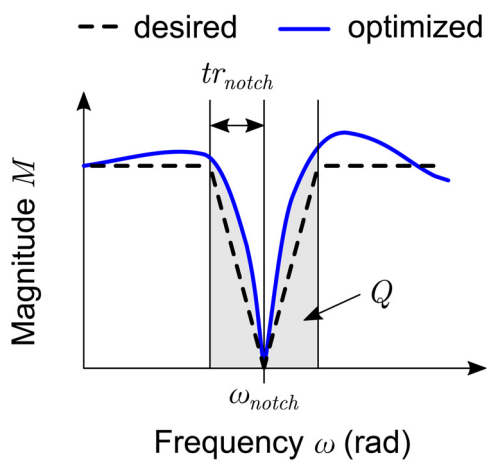

Fig. 4 Calculation of the area Q to determine the notch quality

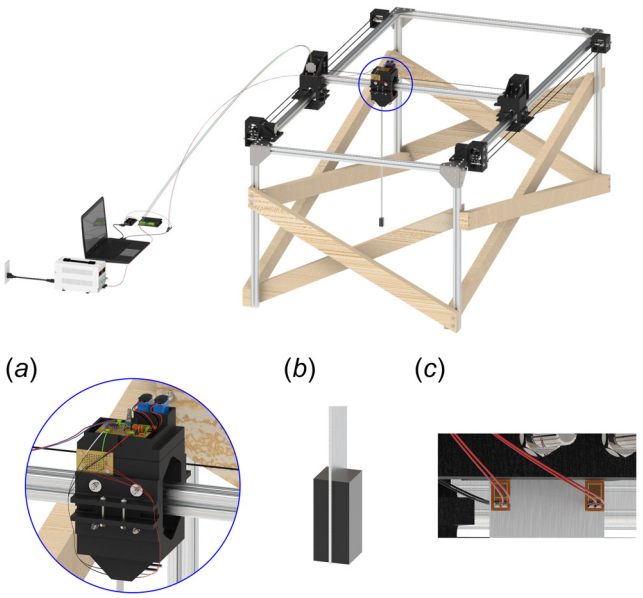

Fig. 5 Experimental setup of the gantry crane: (*a*) amplifier module, (*b*) tip mass, and (*c*) strain gauges

where i, K, Φ, and T are the ith mode, coefficients of the eigenfunction, eigenfunction, and temporal solution, respectively. Equations (19)–(22) can be written in a matrix form as shown in Eq. (25)

$$\mathcal{C}^{\mathrm{T}}\mathcal{A} = \mathbf{0} \tag{25}$$

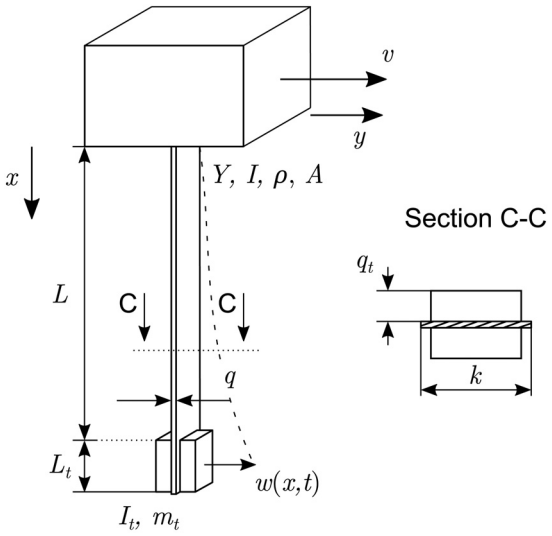

Fig. 6 Trolley model with a clamped beam and tip mass at the free end of the beam

Fig. 7 Mode shapes of a clamped beam with a tipped mass

$$\mathcal{C} = \begin{bmatrix} 1 & 0 & \cosh(\lambda_i) - a_i \sinh(\lambda_i) - c_i \cosh(\lambda_i) & \sinh(\lambda_i) + b_i \cosh(\lambda_i) + c_i \sinh(\lambda_i) \\ 1 & 0 & -\cos(\lambda_i) + a_i \sin(\lambda_i) - c_i \cos(\lambda_i) & \sin(\lambda_i) + b_i \cos(\lambda_i) - c_i \sin(\lambda_i) \\ 0 & 1 & \sinh(\lambda_i) - a_i \cosh(\lambda_i) - c_i \sinh(\lambda_i) & \cosh(\lambda_i) + b_i \sinh(\lambda_i) + c_i \cosh(\lambda_i) \\ 0 & 1 & -\sin(\lambda_i) - a_i \cos(\lambda_i) - c_i \sin(\lambda_i) & -\cos(\lambda_i) + b_i \sin(\lambda_i) + c_i \cos(\lambda_i) \end{bmatrix}_{4\times4} \tag{26}$$

where $\mathcal{A} = [K_{1,i}\, K_{2,i}\, K_{3,i}\, K_{4,i}]^{\mathrm{T}}, a_i = \left(\left(I_t + m_t\left(L_t^2/4\right)\right)\lambda_i^3\right)/\left(\rho A L^3\right)$, $b_i = m_t\lambda_i/(\rho A L)$, and $c_i = m_t L_t \lambda_i^2/\left(2\rho A L^2\right)$. To arrive at a nontrivial solution for Eq. (25), a λ_i can be computed by requiring the determinant of $\mathcal{C}$ to be zero. Then, the natural frequency can be calculated via

$$\omega_{n,i} = \left(\frac{\lambda_i}{L}\right)^2 \sqrt{\frac{YI}{\rho A}}; \quad f = \frac{\omega_{n,i}}{2\pi} \tag{27}$$

Using Eqs. (19), (20), and (22) lead to eigenfunctions given by the following equation:

$$\Phi_i(x) = \left[\frac{-\cosh(\lambda_i) - b_i \sinh(\lambda_i) - c_i \cosh(\lambda_i) - \cos(\lambda_i) + b_i \sin(\lambda_i) + c_i \cos(\lambda_i)}{\sinh(\lambda_i) + b_i \cosh(\lambda_i) + c_i \sinh(\lambda_i) - \sin(\lambda_i) - b_i \cos(\lambda_i) + c_i \sin(\lambda_i)} \ldots \right.$$
$$\left. \left(\cosh\left(\frac{\lambda_i x}{L}\right) - \cos\left(\frac{\lambda_i x}{L}\right)\right) \ldots \ldots + \sinh\left(\frac{\lambda_i x}{L}\right) - \sin\left(\frac{\lambda_i x}{L}\right)\right] K_{3,i} \tag{28}$$

Since the system is a self-adjoint distributed parameter system, it can be shown that the eigenfunctions (mode shapes) are orthogonal. The scaling parameters $K_{3,i}$ can be selected to make the eigenfunctions orthonormal. The mode shapes of the clamped beam with the tipped mass at the end can be seen in Fig. 7 which were generated by ANSYS and match well with the analytical mode shapes used in this paper. The Supplemental Materials on the ASME Digital Collection provides the details of the orthonormalization of the mode shapes. The coefficients K_3 for the first three modes are: [2.570, 3.332, 3.298].

3.2 Sensing and System Identification. The static Euler–Bernoulli beam given in Eq. (18) with a tip load Q_t and clamped free boundary conditions reduces to

$$YI\frac{\partial^4 w(x)}{\partial x^4} = 0 \Rightarrow w(x) = \frac{Q_t}{6YI}\left(3Lx^2 - x^3\right) \tag{29}$$

and the surface strain for a beam of thickness q is

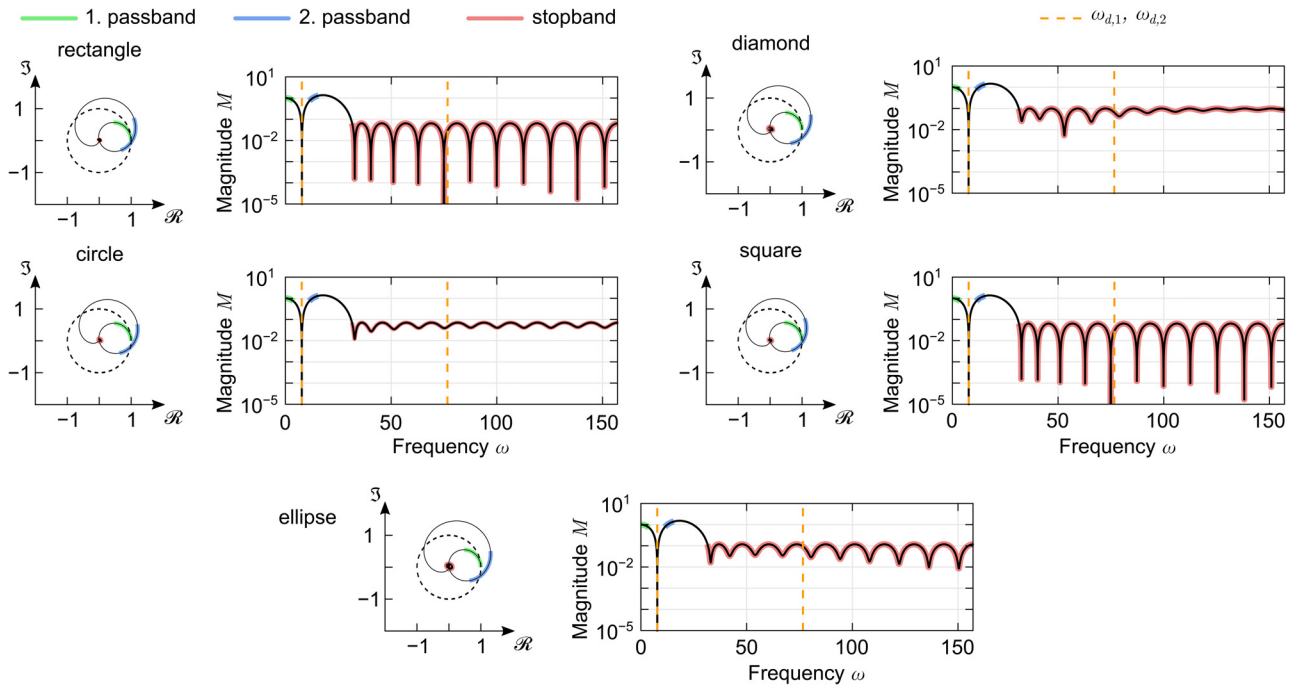

Fig. 8 Different cost functions with the FIR filter in the complex plane and the respective magnitude response (Color version online)

$$\epsilon(x) = -\frac{q}{2}\frac{\partial^2 w(x)}{\partial x^2} = -\frac{qQ_t}{2YI}(L-x) \tag{30}$$

$$= -\frac{3qw(L)}{2L^3}(L-x) = \xi_1 U + \xi_2 \tag{31}$$

which represents a linear mapping between the tip displacement $w(L)$ and the strain at any location x. It should be noted that a bias ξ_2 is included in the model since the measured voltage U is only positive and the zero strain corresponds to a nonzero voltage. For the strain gauge located at $x = 0.01$ m, we have

$$\epsilon(0.01) = -\frac{3qw(L)}{2L^3}(L-0.01) = \xi_1 U + \xi_2 \tag{32}$$

The highlighted part of Eq. (32) is used to map voltage to strain via various known tip displacements $w(L)$. Additional details for the mapping between measured voltage and displacement is provided in the Supplemental Materials on the ASME Digital Collection. The parameters in Eq. (32) are $\xi_1 = -6.9332e^{-4}$ and $\xi_2 = 5.4220e^{-7}$. The time series data from the strain gauge can now be used to estimate the kinetic and potential energy resident in the modes of the beam. The kinetic and potential energies of the beam are [24]

$$\begin{aligned} E_{\text{kin}}(t) = &\frac{1}{2}\int_0^L \rho A(\dot{y} + \dot{w}(x,t))^2 dx \ldots \\ &\ldots + \frac{1}{2} m_t \left(\dot{y} + \dot{w}(L,t) + \frac{L_t}{2}\dot{w}'(x,t)|_{x=L}\right)^2 \ldots \\ &\ldots + \frac{1}{2} I_t \left(\dot{w}'(x,t)|_{x=L}\right)^2 \end{aligned} \tag{33}$$

$$E_{\text{pot}}(t) = \frac{1}{2}\int_0^L YI\left(\frac{\partial^2 w(x,t)}{\partial x^2}\right)^2 dx \tag{34}$$

For a point-to-point maneuver, the residual energy can be used as a performance metric to gauge the deviation from the desired position of rest. At the end of the maneuver, i.e., $t = t_f$, the stepper motor ensures that the velocity of the trolley is zero. Substituting $t = t_f$ and $\dot{y} = 0$ into Eqs. (33) and (34), the residual energy can be determined. Assuming that three modes capture the dominant energy content, the measured strain for all time $t > t_f$ is approximated as

$$\epsilon(0.01, t) = -\frac{q}{2}\sum_{i=1}^{3}\frac{\partial^2 \Phi_i(x)}{\partial x^2}\bigg|_{x=0.01} T_i(t) \tag{35}$$

which permits approximating the deflection as

$$w(x,t) = \sum_{i=1}^{3}\Phi_i(x)\underbrace{\left(C_i e^{-\zeta_i \omega_{n,i} t}\sin(\omega_{d,i} t + \alpha_i)\right)}_{T_i(t)} \tag{36}$$

The curve fitting process assumes that the identified damping ratios $\zeta_1 = 0.002675$ and $\zeta_2 = 0.002900$ are constant, while C_1 to C_3 and α_1 to α_3 as well as L and ζ_3 are optimized for. The curve fitting process is posed as a least squares problem between the measured strain represented by Eq. (32) and the estimated strain in Eq. (35) which assumes ideal clamped geometric boundary conditions as represented in Eqs. (19) and (20). Note that optimizing for L might seem redundant for the current curve fitting process but will be important for robustness studies. The damping ratio ζ_3 is optimized because it is rather difficult to identify from the frequency response function. The method presented in this section permits identifying parameters from the measured strain and consequently computing the energy contribution of each mode.

Subjecting the system to a pulse input, the strain gauge measurement is used to identify the following natural frequencies and damping ratios for the first two modes: $f_{n,1} = 1.2277$ Hz, $f_{n,2} = 12.1974$ Hz, $\zeta_1 = 0.002675$, and $\zeta_2 = 0.002900$. The corresponding geometric and material properties of the beam are: thickness $q = 0.0016$ m, length $L = 0.72 - L_t$ m, width $k = 0.0295$ m, Young's modulus $Y = 69 \times 10^9$ Pa, and density $\rho = 2700$ kg/m^3. The tip mass has the following parameters: thickness $q_t = 0.0123$ m, length $L_t = 0.0441$ m, and mass $m_t = 0.0821$ kg.

4 Simulation and Experimental Results

This section presents the results from simulations, which are validated with experiments. A rectangular pulse serves as the

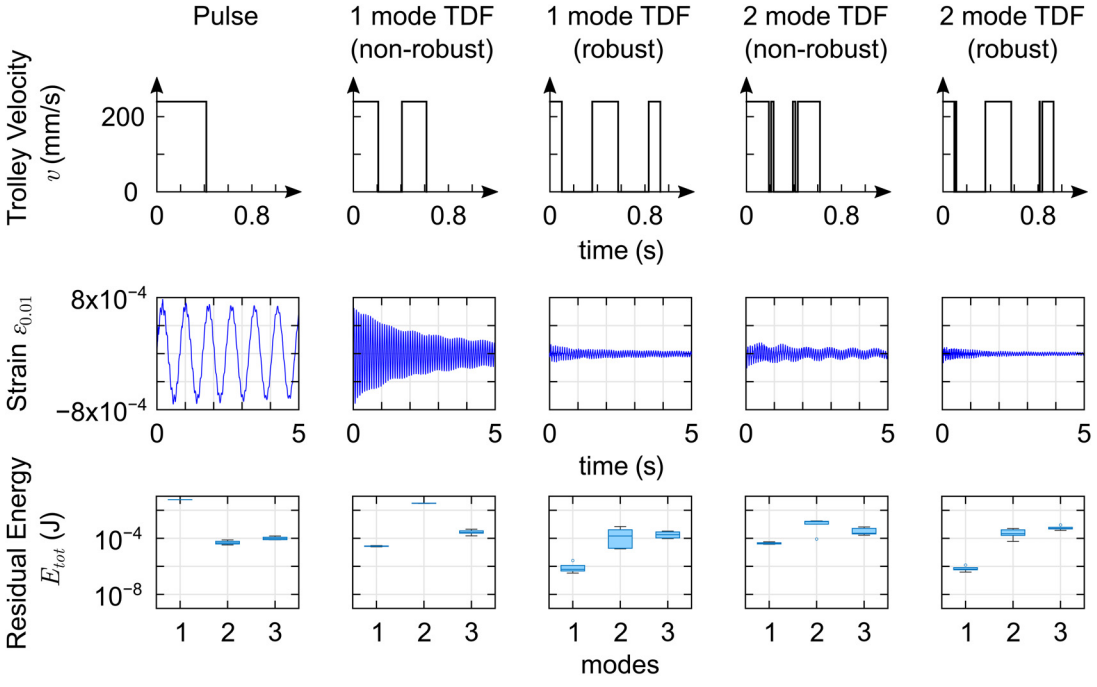

Fig. 9 Experimental results for the residual energy of first, second, and third modes when a rectangular pulse input or velocity constrained TDFs are applied

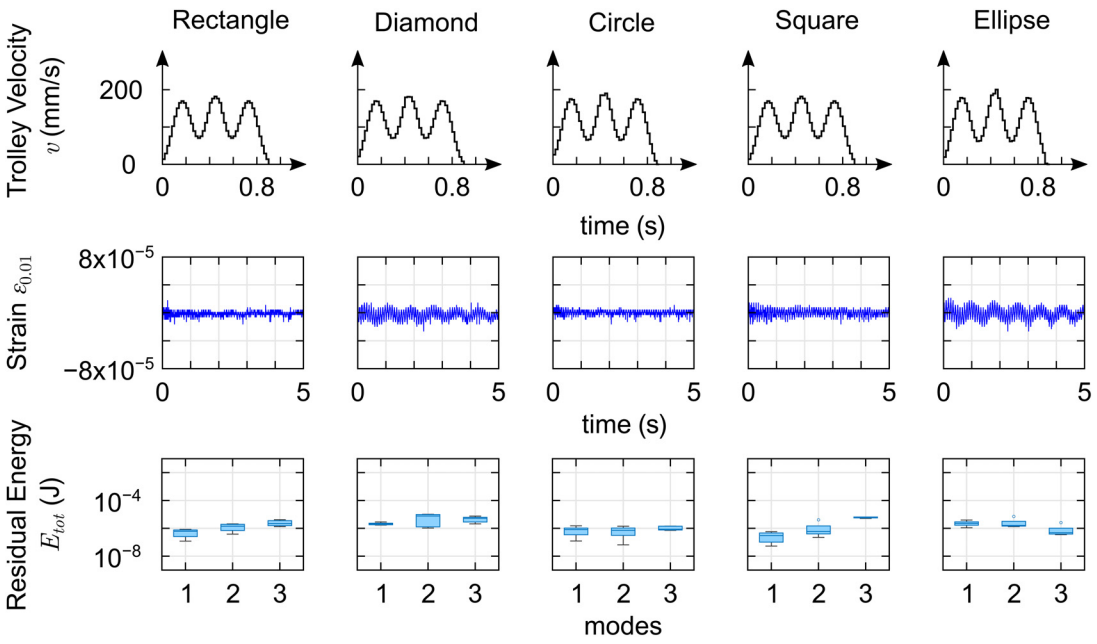

Fig. 10 Experimental results for the residual energy of first, second, and third modes for various convex optimized low-pass FIR filters presented in Fig. 8

velocity reference input and various open loop filtering techniques are used to shape the pulse input. It should be noted that the TDFs are designed with knowledge about the velocity constraint and the objective being time-optimality. In the end of this section, a robustness study related to uncertainty of the first mode is performed.

4.1 Comparison: Rectangular Pulse Input, Time-Delay Filters, and Finite Impulse Response Filters. Nonrobust and a robust single mode TDFs are designed to solely cancel the first mode ($\omega_{n,1} = 7.7139$ rad/s). To additionally cancel the second mode at $\omega_{n,2} = 76.6379$ rad/s, nonrobust and robust 2 mode TDFs are synthesized. Here robustness is ensured for uncertainties in $\omega_{n,1}$ and $\omega_{n,2}$. For the FIR filter design, we choose: $N = 25$, $L = 15N$, $T_s = 0.02$, $\text{tr}_{\text{notch}} = 2\%\ \omega_{\text{final}}$, $\text{tr} = 10\%\ \ \omega_{\text{final}}$, $\omega_{\text{notch}} = \omega_{n,1}\sqrt{1-2\zeta_1^2}$. The stopband starts at 5 Hz ($\omega = 10\pi$ rad/s) which places the second mode in the stopband. The weights are selected as $W_p = 1$ and $W_s = 10$. Figure 8 illustrates the frequency response functions when various convex shapes are used to enclose the permissible magnitudes of the FIR filter for various frequencies in the range $\omega_l \in [0, \pi]$. Each FIR filter is plotted in the complex plane and in a magnitude response as a function of frequency. The green and blue highlights correspond to the passbands and the stopband is highlighted in red. The nonhighlighted parts of the graphs correspond to the transition zones. The vertical dashed lines correspond to the location of the first two natural frequencies of the beam, where the first mode is targeted with a notch, while the second mode is relegated to the stopband without any explicit constraint imposed at that frequency. It is interesting to note that the rectangular and square case seem to result in a comb filter characteristic in the stopband. For the rectangular, circle, and square FIR cost function, the second mode is serendipitously located at a local minimum in the magnitude response. In contrast, the diamond and elliptical magnitude response show the second mode is less attenuated. To evaluate the notch quality, we use Eq. (17) and obtain the following results: $Q_{n,\text{rectangle}} = 0.3238$, $Q_{n,\text{diamond}} = 0.3281$, $Q_{n,\text{circle}} = 0.3244$, $Q_{n,\text{square}} = 0.3238$, and $Q_{n,\text{ellipse}} = 0.3303$, showing that the normalized area is smaller in the rectangle, circle, and square than in the diamond and ellipse case.

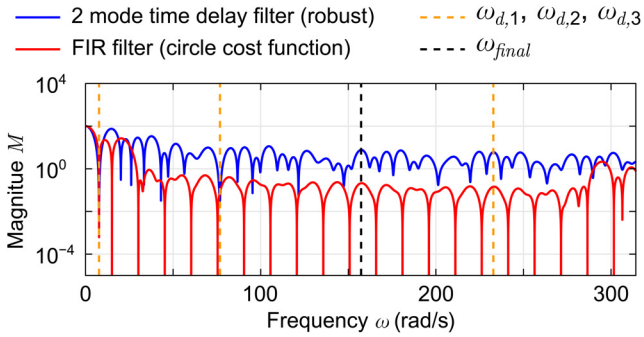

Fig. 11 Comparison between a robust 2 mode TDF and an FIR filter (circle cost function) with 25 elements

For a final displacement of 10.08 cm, a rectangular pulse with $v_{\max} = 240$ mm/s is applied for 0.42 s and passed through the TDFs and FIR filters. For each filter, five experiments were conducted. From Fig. 9, it can be seen that the pulse input creates the largest oscillations followed by the nonrobust single mode TDF, for which the box and whisker chart are confirming that most of the residual energy is resident in the second mode. The least oscillation of all TDFs is related to the robust 2 mode TDF, where it is visible that mostly the third mode is responsible for the residual vibrations. Each FIR filters introduces $T_s \times N = 0.5$ s delay, resulting in a final maneuver time of 0.92 s. Applying different cost functions for the FIR filter design reveals in Fig. 10 that the first mode gets largely attenuated in the rectangle, circle, and square case. The diamond and ellipse case show marginally greater oscillations in the first mode, which can be confirmed by the box and whisker chart. Furthermore, the diamond and ellipse FIR filters show that the second mode gets more excited than in the other cases. The experimental results in Fig. 10 are consistent with the theoretical results from Fig. 8. It is clear that the FIR filters have a lower total residual energy than any TDF (note the scale of the strain is one order lower than for the TDFs). This is not surprising since the TDFs target specific modes, while the FIR filter include a stopband and any unmodeled/uncontrolled mode in the stopband will be better attenuated. In other words, the TDFs are agnostic to the existence of the third or fourth mode and the staircase structure of the time-delay filtered signals can excite unmodeled modes. Figure 11 illustrates the frequency response function of the robust two-mode TDF and a FIR filter

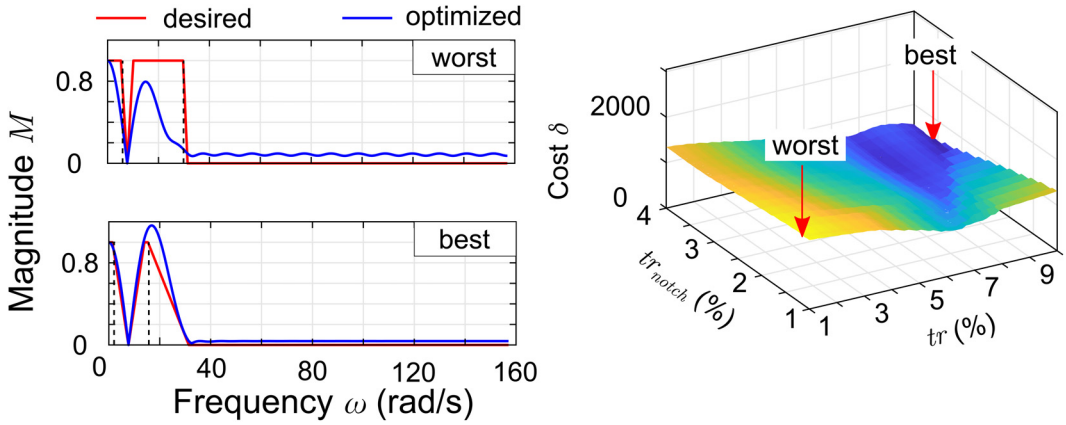

Fig. 12 Cost $\delta = ||\boldsymbol{W}(\omega_l)(\boldsymbol{\Gamma}(\omega_l)\boldsymbol{h} - \boldsymbol{b}_i(\omega_l))||_2$ for a variation of tr_{notch} and tr

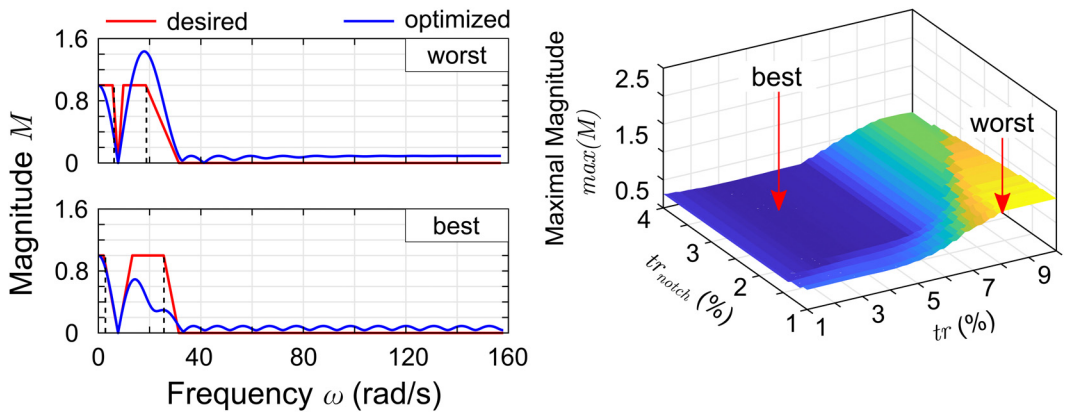

Fig. 13 Magnitude for $\omega \geq \omega_{n,1}$ for a variation of tr_{notch} and tr

designed with a circular cost function. ω_{final} is the final frequency until which the FIR filter is optimized for. It is evident that the magnitude spectrum in the stopband is significantly greater for the TDF relative to the FIR filter.

4.2 Changing the Transition Band Width. The transition width between passband and notch (tr_{notch}) or between passband and stopband (tr) plays an important role in the filter design process. A very narrow transition band leads to undesirable peaks, known as the Gibbs phenomena or might just lead to poor tracking of the desired magnitude response. To analyze the impact of the transition band's influence on how well the magnitude plot tracks the desired frequency response function, both tr_{notch} and tr are changed over a grid. The only change compared to Sec. 4.1 is that we choose $N = 30$. In Fig. 12, a surface plot of δ, the maximum difference (L_2 norm) between the FIR–FRF and the desired FRF, over the variation of the tr_{notch} and tr is illustrated. δ is calculated for 10,000 equally spaced frequency samples from 0 to ω_{final}. The plotted variable along the z-axis is the variation of the L_2 norm. It should be noted that tr_{notch} and tr are presented as a percent values of ω_{final}, the final frequency in the frequency spectrum. A trend which can be observed is that the tracking becomes better as tr becomes greater. It is interesting to note that tr_{notch} does not need to be at its largest value to achieve the best tracking for the magnitude. The worst magnitude tracking occurs when both transition band widths are very small, matching the aforementioned Gibbs phenomena. Figure 13 illustrates the variation of the magnitude peak of the FIR–FRF for $\omega \geq \omega_{notch}$, where it can be observed that a narrower tr_{notch} leads to a greater magnitude and therefore a greater peak. On the other hand it can be seen that the smallest peak is obtained at $tr_{notch} = 3.15\%$ and $tr = 3.7\%$. As it can be seen on the left side of Fig. 13, the smallest magnitude peak does not mean that the tracking error is minimized.

4.3 Optimal Weights, Wider Notch, and Robustness to Uncertainties. To enhance robustness around the first mode $\omega_{n,1}$, a stopband is created around ω_{notch}, instead of solely enforcing a notch with $M_d(\omega_{notch}) \leq 1e^{-5}$. In four different scenarios which are (a) $\omega_{notch} \pm 0.2\pi$, (b) $\omega_{notch} \pm 0.6\pi$, (c) $\omega_{notch} \pm \pi$ with $N = 30$, and (d) $\omega_{notch} \pm \pi$ with $N = 50$ a notch-stopband is designed. Other than changing parameter N all FIR parameters are used as in Sec. 4.1. Three different weight parameters are considered, where W_p is the passband, W_n is the notch-stopband, and W_s is the stopband for higher frequencies. In conjunction with the filter coefficient optimizer, another optimizer endeavors to identify the optimal weight distribution of W_p, W_n, and W_s, which are not influenced by their value, and rather by their respective ratio. For our optimization strategy, we require $W_p + W_n + W_s = 1$. δ is the L_2 norm between the desired and optimized magnitude response. Figure 14 in the top row illustrates the cost as a function of the weights for all four cases. The optimal values for the weights for $[W_p, W_n, W_s]$ are $[0.0115, 0.1006, 0.8879]_{a)}$, $[0.0121, 0.0278, 0.9601]_{b)}$, $[0.0119, 0.0181, 0.9710]_{c)}$, and $[0.0120, 0.0573, 0.9227]_{d)}$. For cases (a)–(c), it can be observed that a wider notch results in the notch moving toward higher frequencies in the magnitude response. The optimal weight on the passband is almost constant but the weight on the notch is decreasing as the desired notch becomes wider, which is a weight shift from W_n to W_s. The normalized areas for the notches are: $Q_{n,a)} = 0.3519$, $Q_{n,b)} = 0.4357$, and $Q_{n,c)} = 0.5038$, where the lower notch quality when transitioning from (a) to (c) stems from the constraint of using only $N = 30$ coefficients, which results into

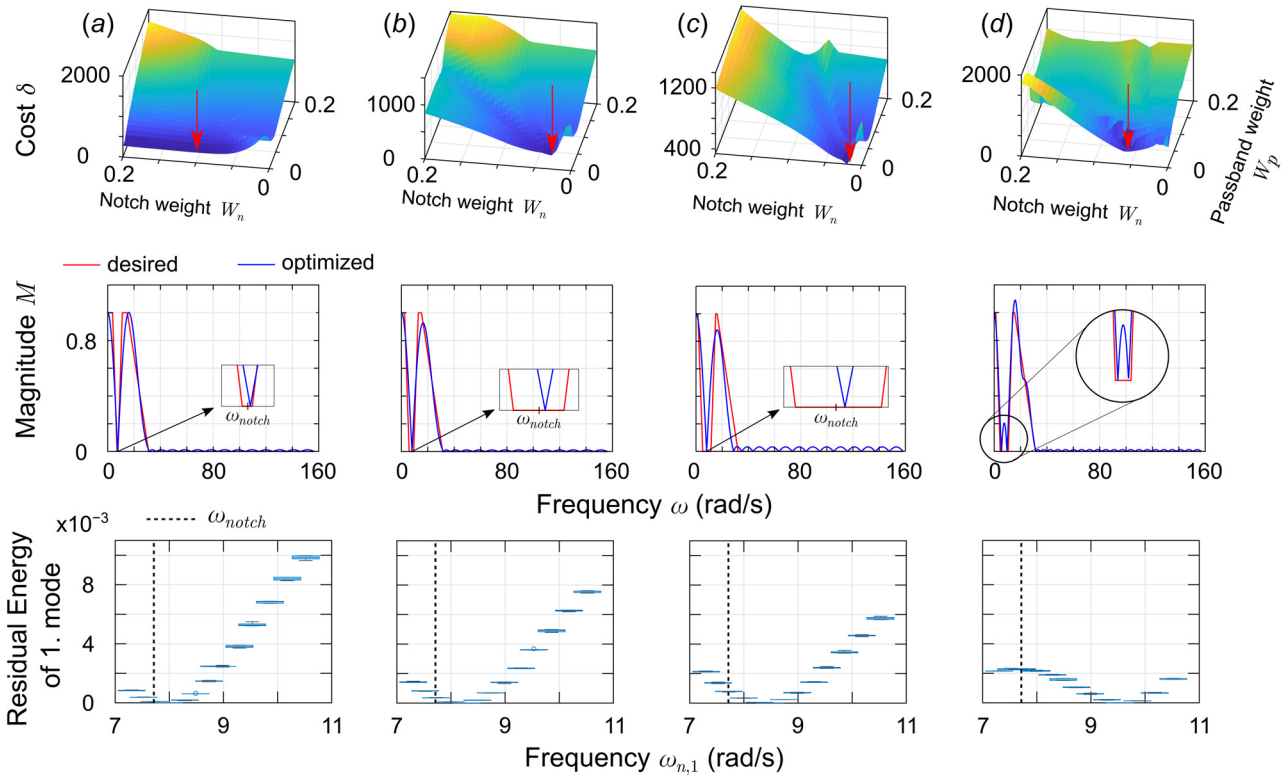

Fig. 14 Simulation (top and middle) and experimental results (bottom). Notch-stopband enforced for: (*a*) $\omega_{notch} = \pm 0.2\pi$, (*b*) $\omega_{notch} = \pm 0.6\pi$, (*c*) $\omega_{notch} = \pm\pi$ for $N = 30$, and (*d*) $\omega_{notch} = \pm\pi$ for $N = 50$.

only one constraint used to enforce the stopband, resulting in deterioration in the quality of the notch. In case (d) the inset shows that the filter optimizer leads to a minimax design in the notch, which provides robustness toward uncertainty around ω_{notch}, e.g., referring to uncertainties in the first mode. The minimax design offers the best design for a worst-case scenario and the normalized area of the notch is: $Q_{n,d)} = 0.3638$, which is 27.79% lower than the FIR filter in (c).

This observation is worthwhile exploring with the experimental setup described in Sec. 3. Since the notch refers to the first mode of the beam structure, it is of interest to determine the residual energy of the first mode. Referring to Fig. 6, uncertainty in the modal frequencies can be realized by sliding the tip mass in x-direction, which changes L, the effective length of the beam. Figure 14 in the bottom row illustrates the residual energy of the first mode for the FIR filters. Each box and whisker chart contains 65 samples. In total, 13 different stages of the tip mass were tested, where it should be mentioned that at the lower frequency end the beam structure is constrained because the tip mass cannot be placed beyond the end of the beam ($x = 0.72$ m). With the help of Eqs. (33) and (34), each experimental result has to undergo a curve fitting process to determine the contribution of each mode in the measured signal. Figure 14 in the bottom row confirms with the subfigures (*a*)–(*c*), the theoretical observed results that the notch is moving toward higher frequencies. Case (c) has generally the lowest residual energies over the uncertain space. Case (d) which led to a minimax design shows that the residual energy of the first mode follows the magnitude response pattern as in the numeric study. The low residual energy of the first mode confirms the robustness of the minimax design over the uncertain domain.

5 Conclusion

This paper formulates a convex optimization problem to design FIR filters to cater to rest-to-rest maneuvers for systems with uncertain underdamped modes and unmodeled high frequency modes. To test the FIR designs, a beam with a tip mass is attached to a moving trolley to emulate point-to-point maneuvers of a flexible structure. Velocity-constrained time-optimal controllers are compared to FIR filters with five different cost functions: rectangle, diamond, circle, square, and ellipse. FIR filters perform better than TDFs in terms of residual energy. Several scenarios are simulated with varying numbers of filter elements, transition widths, and weights. A robustness study in the notch area demonstrates the ability to handle uncertainties in the first mode, such as changes in the tip mass location on a beam. A minimax design is created in the notch area and proved to be more effective than other methods when the first mode of the system is perturbed. The authors introduce the normalized notch area of the magnitude response as a tool to quickly compare filters for robustness. Future research will explore adding more than one robust notch for different system modes. The experiments confirm that FIR filters may take slightly longer for maneuvers but excel at vibration suppression compared to TDFs in the presence of high-frequency dynamics and uncertain modal parameters.

Acknowledgment

The authors acknowledge the support of this work by the U.S. National Science Foundation through CMMI Award No. 2021710. We would like to thank Professor Armstrong, Anthony Olivett, and Amit Bhayadia for the help with the hardware and helpful discussions.

Funding Data

- Directorate for Engineering, CMMI (Award No. 2021710; Funder ID: 10.13039/100000084).

Data Availability Statement

The datasets generated and supporting the findings of this article are obtainable from the corresponding author upon reasonable request.

References

[1] Heertjes, M., Hennekens, D., and Steinbuch, M., 2010, "MIMO Feed-Forward Design in Wafer Scanners Using a Gradient Approximation-Based Algorithm," Control Eng. Pract., **18**(5), pp. 495–506.

[2] Bruijnen, D., and van Dijk, N., 2012, "Combined Input Shaping and Feedforward Control for Flexible Motion Systems," Proceedings of the 2012 American Control Conference (ACC), Montreal, QC, Canada, June 27–29, pp. 2473–2478.

[3] Heertjes, M. F., Butler, H., Dirkx, N. J., van der Meulen, S. H., Ahlawat, R., O'Brien, K., Simonelli, J., Teng, K.-T., and Zhao, Y., 2020, "Control of Wafer Scanners: Methods and Developments," Proceedings of the 2020 American Control Conference (ACC), Denver, CO, July 1–3, pp. 3686–3703.

[4] Singhose, W. E., Porter, L. J., and Seering, W. P., 1997, "Input Shaped Control of a Planar Gantry Crane With Hoisting," Proceedings of the 1997 American Control Conference (Cat. No. 97CH36041), Albuquerque, NM, June 6, pp. 97–100.

[5] Lange, F., Werner, J., Scharrer, J., and Hirzinger, G., 2010, "Assembling Wheels to Continuously Conveyed Car Bodies Using a Standard Industrial Robot," Proceedings of the 2010 IEEE International Conference on Robotics and Automation, Anchorage, AK, May 3–7, pp. 3863–3869.

[6] Peláez, G., Alonso, C., Rubio, H., and García-Prada, J. C., 2023, "Performance Analysis of Input Shaped Model Reference Adaptive Control for a Single-Link Flexible Manipulator," J. Vib. Control, epub.

[7] Singh, T., 2010, *Optimal Reference Shaping for Dynamical Systems: Theory and Applications*, CRC Press, Boca Raton, FL.

[8] Singh, T., and Vadali, S. R., 1994, "Robust Time-Optimal Control: A Frequency Domain Approach," J. Guid., Control, Dyn., **17**(2), pp. 346–353.

[9] Singh, T., and Vadali, S. R., 1995, "Robust Time-Delay Control of Multimode Systems," Int. J. Control, **62**(6), pp. 1319–1339.

[10] Singer, N. C., and Seering, W. P., 1990, "Preshaping Command Inputs to Reduce System Vibration," ASME J. Dyn. Syst., Meas., Control, **112**(1), pp. 76–82.

[11] Murphy, B. R., and Watanabe, I., 1992, "Digital Shaping Filters for Reducing Machine Vibration," IEEE Trans. Rob. Autom., **8**(2), pp. 285–289.

[12] Parks, T., and McClellan, J., 1972, "Chebyshev Approximation for Nonrecursive Digital Filters With Linear Phase," IEEE Trans. Circuit Theory, **19**(2), pp. 189–194.

[13] Davidson, T., 2010, "Enriching the Art of FIR Filter Design Via Convex Optimization," IEEE Signal Process. Mag., **27**(3), pp. 89–101.

[14] Karam, L. J., and McClellan, J. H., 1995, "Complex Chebyshev Approximation for FIR Filter Design," IEEE Trans. Circuits Syst. II: Express Briefs, **42**(3), pp. 207–216.

[15] Bae, H. S., and Gerdes, J. C., 2003, "Command Modification Using Input Shaping for Automated Highway Systems With Heavy Trucks," Proceedings of the 2003 American Control Conference, Denver, CO, June 4–6, pp. 54–59.

[16] Bae, H. S., 2004, "Command Modification Using Input Shaping for Automated Highway Systems With Heavy Trucks," Ph.D. thesis, Stanford University, Stanford, CA.

[17] Boyd, S. P., and Vandenberghe, L., 2004, *Convex Optimization*, Cambridge University Press, Cambridge, UK.

[18] Aggarwal, A., Rawat, T. K., Kumar, M., and Upadhyay, D. K., 2015, "Optimal Design of FIR High Pass Filter Based on L1 Error Approximation Using Real Coded Genetic Algorithm," Eng. Sci. Technol., Int. J., **18**(4), pp. 594–602.

[19] Preuss, K., 1989, "On the Design of FIR Filters by Complex Chebyshev Approximation," IEEE Trans. Acoust., Speech, Signal Process., **37**(5), pp. 702–712.

[20] Lai, X., Zuo, Y., Guo, Y., and Peng, D., 2009, "A Complex-Error and Phase-Error Constrained Least-Squares Design of FIR Filters With Reduced Group Delay Error," Proceedings of the 2009 Chinese Control and Decision Conference, Guilin, China, June 17–19, pp. 1967–1972.

[21] Qin, F., 1997, "A Practical Method for Designing FIR Digital Filters in the Complex Domain," IEEE Trans. Signal Process., **45**(8), pp. 2092–2096.

[22] Singh, T., 1991, "Dynamics and Control of Flexible Arm Robots," Ph.D. dissertation, University of Waterloo, Waterloo, ON, Canada.

[23] Inman, D. J., 2014, *Engineering Vibration*, 4th ed., Pearson, Boston, MA.

[24] Erturk, A., and Inman, D. J., 2011, *Piezoelectric Energy Harvesting*, Wiley, Chichester, UK.